



HAL
open science

Weak anvil cloud area feedback suggested by physical and observational constraints

Brett Mckim, Sandrine Bony, Jean-Louis Dufresne

► **To cite this version:**

Brett Mckim, Sandrine Bony, Jean-Louis Dufresne. Weak anvil cloud area feedback suggested by physical and observational constraints. *Nature Geoscience*, 2024, 17 (5), pp.392-397. 10.1038/s41561-024-01414-4 . hal-04694494

HAL Id: hal-04694494

<https://hal.sorbonne-universite.fr/hal-04694494v1>

Submitted on 11 Sep 2024

HAL is a multi-disciplinary open access archive for the deposit and dissemination of scientific research documents, whether they are published or not. The documents may come from teaching and research institutions in France or abroad, or from public or private research centers.

L'archive ouverte pluridisciplinaire **HAL**, est destinée au dépôt et à la diffusion de documents scientifiques de niveau recherche, publiés ou non, émanant des établissements d'enseignement et de recherche français ou étrangers, des laboratoires publics ou privés.



Distributed under a Creative Commons Attribution 4.0 International License

Weak anvil cloud area feedback suggested by physical and observational constraints

Received: 26 May 2023

Brett McKim^{1,2}✉, Sandrine Bony¹ & Jean-Louis Dufresne¹

Accepted: 29 February 2024

Published online: 1 April 2024

 Check for updates

Changes in anvil clouds with warming remain a leading source of uncertainty in estimating Earth's climate sensitivity. Here we develop a feedback analysis that decomposes changes in anvil clouds and creates testable hypotheses for refining their proposed uncertainty ranges with observations and theory. To carry out this storyline approach, we derive a simple but quantitative expression for the anvil area feedback, which is shown to depend on the present-day measurable cloud radiative effects and the fractional change in anvil area with warming. Satellite observations suggest an anvil cloud radiative effect of about $\pm 1 \text{ W m}^{-2}$, which requires the fractional change in anvil area to be about $50\% \text{ K}^{-1}$ in magnitude to produce a feedback equal to the current best estimate of its lower bound. We use quantitative theory and observations to show that the change in anvil area is closer to about $-4\% \text{ K}^{-1}$. This constrains the area feedback and leads to our revised estimate of $0.02 \pm 0.07 \text{ W m}^{-2} \text{ K}^{-1}$, which is many times weaker and more constrained than the overall anvil cloud feedback. In comparison, we show the anvil cloud albedo feedback to be much less constrained, both theoretically and observationally, which poses an obstacle for bounding Earth's climate sensitivity.

Global warming depends on Earth's sensitivity to increased CO_2 , but this sensitivity is tied to how clouds 'feedback' on global warming¹. While recent progress has been made in constraining low-cloud feedbacks^{2,3}, anvil cloud feedbacks are still leading sources of uncertainty in quantifying climate sensitivity^{4,5} despite decades of study^{6–12}. The question thus remains: how do anvil clouds respond to and affect warming?

Changes in anvils were once thought to produce a strong negative climate feedback by acting as a solar thermostat⁶, but the observations that led to this conclusion are no longer considered evidence of such an effect⁷. Then anvils were thought to act as an infrared iris⁸. Criticisms of this study's methodology followed^{9,13,14}, but recent comprehensive assessments still cannot rule out a modest anvil cloud feedback^{4,5}.

These assessments refer to an anvil cloud area (or amount) feedback, but it should be more precisely referred to as the altitude-corrected anvil cloud feedback (hereafter, the anvil cloud feedback) since it results from changes in area and optical depth but not changes in altitude, which are considered in a separate feedback¹⁵. Such decompositions are arbitrary because climate is unchanged by how it is analysed, but the choice is important because it can simplify

interpretations of uncertainty¹⁶. Further decomposition may help constrain the anvil cloud feedback by answering which individual feedback—area or optical depth—truly embodies the uncertainty that obscures estimates of climate sensitivity.

Anvil cloud area is controlled in part by unconstrained microphysics^{17–19} but also by robust thermodynamic principles^{20,21}, which predict a decrease in anvil area with warming as atmospheric static stability increases²¹. This is consistent with observed variability^{22–24} and most simulations²⁵. The resulting area feedback might be small because anvils are radiatively neutral^{7,11,26}. But how neutral must anvil clouds be for the feedback to be small? What if their radiative effect changes with warming? Or if more of Earth is then exposed to the radiative effects of underlying low clouds? These questions limit our ability to constrain the anvil cloud area feedback.

Less is known about how cloud optical depth changes with warming²⁷, but it will manifest in optical properties such as anvil cloud albedo. Changes in albedo might produce an even stronger feedback than changes in area because anvils have a much stronger effect in the short wave than in the net¹¹. But how much does cloud albedo change

¹LMD/IPSL, Sorbonne Université, CNRS, Paris, France. ²Department of Mathematics and Statistics, University of Exeter, Exeter, UK.

✉e-mail: brett.mckim@lmd.ipsl.fr

with warming? And by how much must it change to produce a substantial feedback? These questions call for more quantitative answers before we can conclude which feedback is more uncertain.

We need a physically motivated decomposition that addresses confounding factors such as cloud overlap and distinguishes feedbacks from changes in anvil area and albedo. Since models must contend with representing unconstrained microphysics^{17–19}, we primarily use observations. This rules out using purely model-based cloud feedback decompositions^{28,29}. Cloud-controlling factor analysis, an observation-based method used mostly for constraining low-cloud feedbacks³⁰, requires further study before being suitable for confidently constraining anvil cloud feedbacks. The connection between anvil clouds and their cloud-controlling factors are not as well understood as for low clouds.

In this Article, we derive an analytical cloud feedback decomposition based on the essential physics of cloud radiative effects. When it is combined with cloud observations, we can identify, understand and constrain cloud feedbacks transparently. We adopt a storyline approach³¹ where we examine the driving factors that control a cloud feedback and judge the plausibility of these factors to produce a particular feedback value by comparing with observations and theory derived from process understanding. This approach shows which feedback is constrained and which obscures estimates of climate sensitivity.

Conceptualizing cloud radiative effects

Clouds are complex, but for simplicity we divide them into two types, high (h) and low (l), and subsume their properties into a few parameters obtainable from observations and reanalysis (Extended Data Table 1). They include area fractions f_h, f_l , emission temperatures T_h, T_l and albedos α_h, α_l . Long-wave emissivities are not considered because most clouds have an emissivity close to one³². Clear-sky radiation is distilled to the incoming solar radiation S^\downarrow , surface albedo α_s and outgoing long-wave radiation for a given surface temperature $R_{cs}^{T_s}$. Neglecting atmospheric absorption will bias the surface and cloud albedos to be higher, but this permits the derivation of analytical expressions for cloud radiative effects from high clouds and low clouds C_h, C_l ; cloud-overlap effects m_{th} ; and the top-of-the-atmosphere (TOA) energy balance N . See Fig. 1 for an illustration and Methods for the derivation.

Analytic feedbacks and the storyline approach

Feedbacks are computed by differentiating Earth’s TOA energy balance (Equation (16) minus Equation (14); Methods) with respect to the surface temperature T_s (ref. 33). To start, we have:

$$\lambda \equiv \frac{dN}{dT_s} = \frac{dN_{cs}}{dT_s} + \frac{dC}{dT_s}, \quad (1)$$

where N_{cs} is the clear-sky TOA energy balance and $C = C_h + C_l + m_{th}$ is the net cloud radiative effect from all clouds. Plugging in the expressions for C (Equations (15) and (17); Methods), we arrive at an equation for tropical climate feedbacks:

$$\lambda = \lambda_0 + \sum_{i=h,l} (\lambda_i^{area} + \lambda_i^{temp} + \lambda_i^{albedo}), \quad (2)$$

where λ_0 is the reference response assuming a fixed anvil temperature and fixed relative humidity^{12,34}, and λ_i^{area} , λ_i^{temp} and λ_i^{albedo} are the feedbacks from changes in cloud area, cloud temperature and cloud albedo. See Methods for the derivation.

These analytic expressions serve our storyline approach by transparently and quantitatively relating changes in cloud properties to their radiative feedbacks. A more formal Bayesian framework of hypothesis testing (used in refs. 4,31 to constrain climate sensitivity by

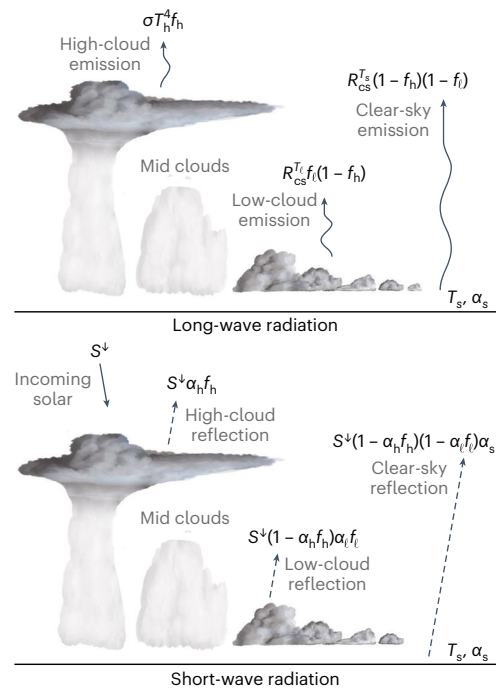


Fig. 1 | Conceptualizing cloud radiative effects. We idealize the vertical cloud profile into two distinct layers that represent anvil clouds and low clouds with random overlap. Equations indicate the domain-averaged contribution of high clouds, low clouds and the surface to TOA energy balance. Their sums in the long wave and short wave are given by Equations (14) and (16), respectively. See Extended Data Table 1 for symbol meanings and values.

reconciling diverse lines of evidence) will not be necessary here because we consider only a process perspective on anvil changes.

The anvil cloud area feedback, λ_h^{area} , comes from collecting terms from equation (1) that involve changes in anvil area df_h/dT_s :

$$\lambda_h^{area} = \frac{d \ln f_h}{dT_s} (C_h + m_{th}). \quad (3)$$

This physically based derivation shows that λ_h^{area} depends on the fractional change in anvil area with warming $d \ln f_h/dT_s$ and the sum of the present-day anvil cloud radiative effect C_h and cloud-overlap effect m_{th} . This aids our storyline approach in two ways. Fractional changes in cloud area are easier to interpret and bound than absolute changes. And although we computed the change in cloud radiative effect with warming, our derivation reveals the area feedback does not depend on the change in radiative effect, but its present-day value.

This means it can be quantified and used to constrain the feedback—the smaller $C_h + m_{th}$ is, the larger $d \ln f_h/dT_s$ has to be to produce a given λ_h^{area} bound. We can probe the plausibility of a given bound by quantifying the observed anvil cloud radiative effect, calculating the change in anvil area required to produce the bound and then comparing the required change in anvil area with the amount expected from theory, simulations and observations. If the expected change in anvil area is much smaller than the required change, then that bound can be refined.

Climatology

Bounding the area feedback requires quantifying the tropically averaged anvil cloud radiative effect and cloud-overlap effect ($C_h + m_{th}$). These quantities are not directly observed and must be inferred from our simple model of cloud radiative effects.

We do this by inputting observations of cloud fraction from CALIPSO, a dataset from a satellite with lidar remote sensing³⁵, clear-sky radiation from CERES, a dataset from radiometers flying on multiple

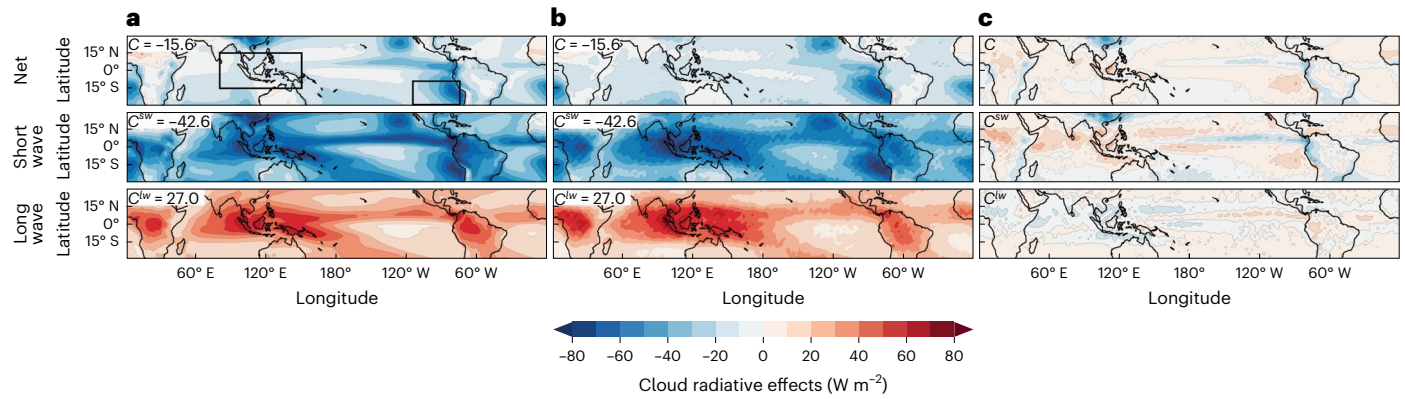


Fig. 2 | Observed net, short-wave and long-wave cloud radiative effects from CERES compared with their inferred counterparts. a, Observed cloud radiative effects. b, Inferred cloud radiative effects. c, Observed – inferred

radiative effects. Tropical mean values are shown in the upper left of each panel. The West Pacific Warm Pool and East Pacific regions are boxed in **a**. The colour bar is the same for all plots.

satellites³⁶, surface temperature from HadCRUT5, a dataset based on measurements from ships, buoys, and weather stations³⁷, and atmospheric temperature from ERA5, a climate reanalysis dataset³⁸, into our expression for the net cloud radiative effect (equations (15) and (17); Methods). Similar to ref. 22, f_h and f_l are identified as the maximum of the observed cloud fraction profile above and below 8 km, respectively, and for an optical depth range between 0.3 and 5.0. This excludes the thickest and thinnest portions of anvil clouds, but the relationship between cloud area and surface warming is robust to the optical depth range considered²². T_h and T_l are the atmospheric temperature at the height of f_h and f_l .

We ensure goodness of fit between the inferred and observed cloud radiative effects by adding a single scaling factor n to the anvil cloud fraction, which accounts for collapsing the anvil cloud fraction profile into a single level (Methods and Extended Data Fig. 1). We treat n as a constant because spatio-temporal variations in the vertical profile of anvil clouds affect the optical depth and hence α_h and α_l , which already capture this variability as they are allowed to vary from year to year. In summary, n , α_h and α_l are tunable parameters to ensure consistency with observations at TOA (see Methods for further details).

We test our idealizations by comparing the observed net, short-wave and long-wave cloud radiative effects (C_{obs} , C_{obs}^{sw} and C_{obs}^{lw}) with their counterparts from the simple model (Fig. 2), which take the spatial fields of cloud fraction, temperature, albedo and clear-sky radiation as inputs. Our model can reproduce spatial patterns of long-wave and short-wave cloud radiative effects, although there are small deviations throughout the tropics: an underestimate of C in the southeast of China and an overestimate of C in the eastern Pacific, next to South America (Fig. 2c). Given the overall close agreement, we consider our model fit for evaluating the tropical anvil cloud area feedback.

The climatological values of tropical quantities used in our calculations are summarized in Extended Data Table 1, and the cloud properties of interest are plotted in Fig. 3. The f_h is maximum in the West Pacific Warm Pool, and f_l is maximum along the East Pacific. Decomposing C into its contributions from different layers reveals that the net C is dominated by C_l . By comparison, the overlap effect m_{th} is much smaller and varies less. The same is true for the high-cloud radiative effect C_h , which exhibits strong cancellation between its short-wave and long-wave components not just in the warm pool^{24,39,40}, but across the tropics.

Constraining the anvil cloud area feedback

We can now constrain the tropical anvil cloud area feedback. To scale our estimate of λ_h^{area} to the global average, we multiply by the area ratio of the tropics and the globe, 1/2.

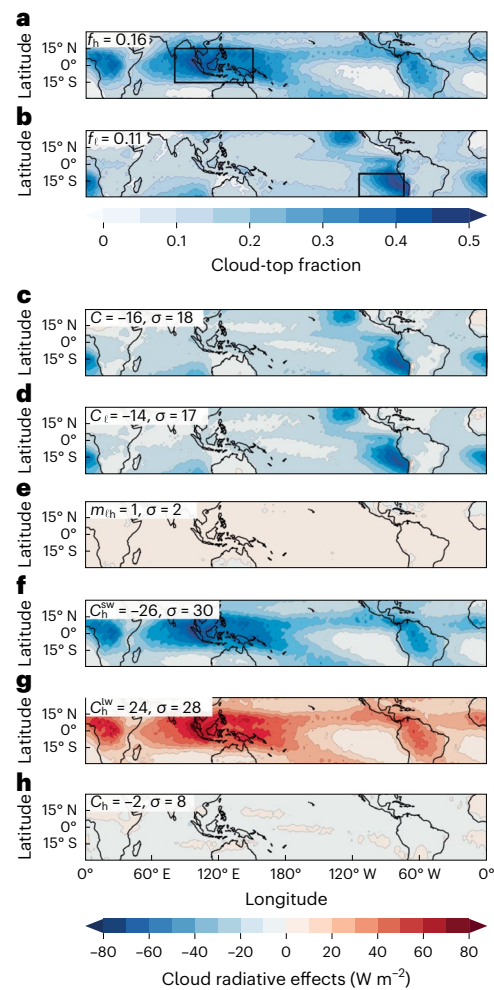


Fig. 3 | Climatological values of tropical quantities. a, b, Effective anvil cloud fraction (a) and low-cloud fraction (b) from CALIPSO. The West Pacific Warm Pool and East Pacific regions are boxed to indicate regions of maximum anvil and low-cloud coverage, respectively. c–h, Inferred cloud radiative effects from Equations (18), (19) and (21). c, Net cloud radiative effect. d, Low cloud radiative effect. e, Cloud overlap effect. f, Shortwave high cloud radiative effect. g, Longwave high cloud radiative effect. h, High cloud radiative effect. Tropical mean values and standard deviations are shown in the upper left of each panel. Refer to Extended Data Fig. 2 to see m_{th} and C_h plotted with a finer colour scale.

$$\langle \lambda_h^{\text{area}} \rangle = \frac{1}{2} \frac{d \ln f_h}{dT_s} (C_h + m_{\text{th}}). \quad (4)$$

The plausible lower bound of $\langle \lambda_h^{\text{area}} \rangle > -0.4 \text{ W m}^{-2} \text{ K}^{-1}$ comes from assuming the anvil cloud feedback in ref. 4 is due to area changes alone. This bound allows the possibility of an overall negative cloud feedback, a necessary ingredient for a climate sensitivity below 1.5 K (ref. 31). Our inferred tropical mean value of $C_h + m_{\text{th}} \approx -1.5 \text{ W m}^{-2}$ implies that $d \ln f_h / dT_s$ must be $\sim 50\% \text{ K}^{-1}$ to achieve this bound. Following our storyline approach, we assess how plausible these cloud changes are by comparing them with the changes expected from theory²¹ and observed interannual variability²².

The stability iris hypothesis²¹ states that anvil cloud fraction f_h is proportional to detrainment from deep convection. Owing to mass conservation, this detrainment is equal to the clear-sky convergence, $\partial_p \omega$, where ω is the subsidence vertical velocity (hPa day^{-1}). If we make the ansatz that $\partial_p \omega$ is proportional to ω at the level of detrainment (h), then the fractional change in anvil area is equal to the fractional change in subsidence velocity at the anvil level:

$$\frac{d \ln f_h}{dT_s} = \frac{d \ln \omega_h}{dT_s}. \quad (5)$$

The subsidence velocity can be written as the quotient of the clear-sky radiative flux divergence in temperature coordinates ($-\partial_T F$) and the difference between actual and dry lapse rates¹⁹:

$$\omega = \frac{-\partial_T F}{1/\Gamma - 1/\Gamma_d}. \quad (6)$$

Given that $\partial_T F$ does not vary with surface temperature⁴¹, if we further assume that Γ_h , the lapse rate at the anvil level, is moist adiabatic, then the change in cloud area can be computed with a few representative numbers. Assuming the surface warms from $T_s = 298 \text{ K}$ to 299 K and the anvil cloud warms from $T_h = 221 \text{ K}$ to anywhere between 221 and 221.4 K (a typical range of anvil warming⁴², which affects the static stability the anvil finds itself in²¹), then we expect that anvils change in area at about

$$\begin{aligned} \frac{d \ln f_h}{dT_s} &= -\frac{d \ln(1/\Gamma_h - 1/\Gamma_d)}{dT_s} \text{ (stability iris)} \\ &\approx -1 \text{ to } -4\% \text{ K}^{-1}, \end{aligned} \quad (7)$$

depending on anvil warming. Despite the simplifications, the result is similar to the mean and standard deviation of large-domain models in RCEMIP (Radiative–Convective Equilibrium Model Intercomparison Project) ($-2 \pm 5\% \text{ K}^{-1}$ for cloud-resolving models, $-2 \pm 4\% \text{ K}^{-1}$ for all models; table S5 of ref. 42).

Now turning to ENSO- (El Niño/Southern Oscillation-) driven interannual variability, we compute annual averages of $\ln f_h$ and T_s (tropical mean surface temperature) from July to June, similar to ref. 22, and plot their scatter in Fig. 4. The line of best fit for this relation gives

$$\frac{d \ln f_h}{dT_s} \approx -7 \text{ to } -11\% \text{ K}^{-1}. \text{ (interannual variability)} \quad (8)$$

This change is larger than our simple estimate and from RCEMIP; it is also larger than the change of $-5\% \text{ K}^{-1}$ inferred from interannual variability in Atmospheric Model Intercomparison Project runs with the Institut Pierre Simon Laplace, Max Planck Institute and National Center for Atmospheric Research models (see figure S3 of ref. 21). However, since all of these estimates of anvil cloud changes are still much smaller than what is required to achieve the lower bound of $\langle \lambda_h^{\text{area}} \rangle = -0.4 \text{ W m}^{-2} \text{ K}^{-1}$, the bounds of the area feedback can be refined.

Care should be taken when inferring the long-term anvil cloud area change from present-day observations. Anvil area is better correlated with upper tropospheric stability than with surface temperature^{22,23}, and surface- and upper-tropospheric warming (and thus changes in

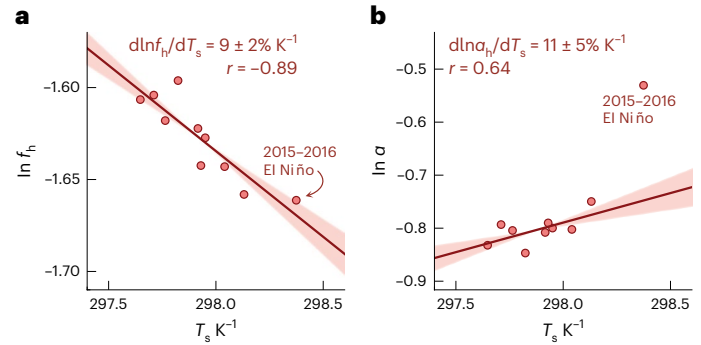


Fig. 4 | Interannual changes in tropical mean anvil cloud area and anvil cloud albedo as a function of surface temperature. **a**, Area change. **b**, Albedo change. Each point represents one year from 2006 to 2016. In each subplot, the slope, correlation of the best fit line and its standard error are shown. Standard error in the slope due to limited sampling is indicated by shading. In **b**, the regression is calculated excluding the 2015–2016 El Niño. See Extended Data Fig. 4 for regression calculated including the El Niño and the regression calculated for low-cloud albedo.

stability) do not always go hand in hand on interannual timescales^{23,43}. ENSO-driven variability is associated with reorganization of deep convection⁴⁴, which may further alter anvil area’s sensitivity to surface temperature. Anvil clouds are about half as sensitive for long-term warming as compared with interannual variability in the Institut Pierre Simon Laplace general circulation model²³, the only model where such analysis has been done.

Given the evidence from theory (equation (7)), observations (equation (8)) and simulations^{21,23,25}, we estimate that anvil cloud area changes at about

$$\frac{d \ln f_h}{dT_s} = -4 \pm 2\% \text{ K}^{-1}. \text{ (best estimate)} \quad (9)$$

We found $C_h + m_{\text{th}} = -1.5 \text{ W m}^{-2}$, but other studies have estimated -4 W m^{-2} (ref. 40), 0.6 W m^{-2} (ref. 17) and 2 W m^{-2} (ref. 45). This is probably due to methodological differences and because anvil clouds have no precise definition. CERES TOA fluxes have their own small uncertainties³⁶, and considering mid-level clouds as distinct entities from low clouds adds an additional uncertainty of 0.5 W m^{-2} (Methods). Therefore, we estimate the anvil cloud radiative effect and cloud-overlap effect to be,

$$C_h + m_{\text{th}} = -1 \pm 3 \text{ W m}^{-2}. \text{ (best estimate)} \quad (10)$$

Using these best estimates in equation (4), we get our best estimate of the anvil area feedback to within one standard deviation:

$$\langle \lambda_h^{\text{area}} \rangle = 0.02 \pm 0.07 \text{ W m}^{-2} \text{ K}^{-1}. \text{ (best estimate)} \quad (11)$$

Overlap effects with low-level clouds are accounted for ($m_{\text{th}} = 0.5 \text{ W m}^{-2}$): they dampen the anvil cloud area feedback by about 25%. Our estimate for the anvil cloud area feedback is positive but ten times smaller in magnitude and three times more constrained than the World Climate Research Programme estimate of $-0.2 \pm 0.2 \text{ W m}^{-2} \text{ K}^{-1}$ for the anvil cloud feedback⁴. We deem the area feedback is now well constrained because its uncertainty is comparable to other assessed cloud feedbacks^{4,5}. Our results provide a rigorous basis to qualitative arguments for a small area feedback^{7,11,26}. What about the anvil cloud albedo feedback?

Uncertainty in the anvil cloud albedo feedback

A substantial feedback could be produced without any change in anvil area^{11,29}. To see why, consider the anvil cloud albedo feedback,

$$\lambda_h^{\text{albedo}} = \frac{1}{2} \frac{d \ln \alpha_h}{dT_s} (C_h^{\text{sw}} + m_{\text{th}}^{\text{sw}}). \quad (12)$$

It follows a form similar to the area feedback but depends on the fractional change in cloud albedo with warming $d \ln \alpha_h / dT_s$, the short-wave anvil cloud radiative effect C_h^{sw} and the short-wave cloud-overlap effect m_{eh}^{sw} (see Methods for derivation).

Given that $C_h^{sw} + m_{eh}^{sw} \approx -25 \text{ W m}^{-2}$ (Extended Data Table 1), producing $\lambda_h^{\text{albedo}} = -0.2 \text{ W m}^{-2} \text{ K}^{-1}$ requires a fractional change in cloud albedo of only 1–2% K^{-1} . How plausible is such a change?

Computing the anvil cloud albedos for each year (Methods), we find $d \ln \alpha_h / dT_s \approx 6\text{--}16\% \text{ K}^{-1}$ and a particularly large increase in albedo during the 2015–2016 El Niño (Fig. 4b) for reasons that are unclear— anvil height and temperature are not as sensitive to El Niño (Extended Data Fig. 3); and changes in low-cloud albedo are more ambiguous than anvil cloud albedo (Extended Data Fig. 4). Such a change implies $\lambda_h^{\text{albedo}} \approx 1/2 \times 10\% \text{ K}^{-1} \times -25 \text{ W m}^{-2} \sim \mathcal{O}(-1) \text{ W m}^{-2} \text{ K}^{-1}$, a large negative feedback, but this should be interpreted carefully.

First, our diagnosed values of cloud albedo may be biased by ignoring clear-sky atmospheric absorption, assuming a spatially uniform cloud albedo, excluding the thickest ($\tau > 5$) and thinnest ($\tau < 0.3$) portions of anvil clouds and assuming a cloud emissivity of 1. We have shown an increase in anvil cloud albedo with warming, whereas another observational study showed anvil cloud thinning with warming and thus a decrease in cloud albedo⁴⁶. Yet another observational study showed ice-water path, a proxy for optical depth, to be non-monotonic with sea surface temperatures⁴⁷.

Second, there is no guarantee that long-term warming will follow interannual warming.

Third, there is no compelling, quantitative understanding of cloud condensate or albedo changes. The cloud albedo response in simulations warrants caution because of large intermodel spreads in climatology of cloud condensate and cloud radiative effects⁴². A precise answer may depend on disentangling the uncertain response of precipitation efficiency with warming^{24,27}.

Fourth, if anvil cloud optical depth is increasing, then long-wave emissivity ϵ_h will increase too and produce a countervailing positive long-wave feedback,

$$\lambda_h^{\text{emissivity}} = \frac{1}{2} \frac{d \ln \epsilon_h}{dT_s} (C_h^{lw} + m_{eh}^{lw}), \quad (13)$$

but with an uncertain magnitude (see Methods for further discussion). The net result of these competing components of the optical depth feedback are unclear, although they might account for the negative anvil cloud feedback found in the observation study⁴⁸ that forms the basis of estimates in comprehensive assessments^{4,5}.

Given the lack of understanding of albedo changes, conflicting observational evidence and a potentially countervailing long-wave anvil emissivity feedback, we conclude the magnitude and uncertainty of the anvil cloud feedback in these previous assessments is embodied primarily by optical depth changes. Convective aggregation may also contribute some uncertainty if it changes anvil optical depth⁴⁹.

Implications of uncertainty

A rigorous assessment of the anvil cloud area feedback was lacking because the confounding factors of cloud overlap and a changing cloud radiative effect on the feedback could not be accounted for. We leveraged the arbitrary nature of feedback decompositions to derive a physically based decomposition that could address these challenges. With it, we constrained the bounds on the anvil cloud area feedback by creating a physical storyline for its previous bounds and then refuting that storyline with observations and theory.

Much attention has been devoted to changes in anvil cloud area, but optical depth changes are now the most uncertain aspect of the anvil cloud response to warming. Focusing on them will promise enhanced returns for constraining climate sensitivity, but doing so with observations alone will be hard because detecting fractional change in

cloud albedo at the precision of 1% K^{-1} nears the limit of active sensor global cloud observing systems⁵⁰.

Constraining these feedbacks will require a mechanistic understanding of how anvil clouds partition themselves into their convective and stratiform components^{11,17}. Pursuing such an understanding would benefit other approaches to constraining anvil cloud optical depth feedbacks, including emergent constraints, model intercomparisons, cloud-controlling factor analysis, process studies and climatological predictors, because confidence in these methods ultimately derives from understanding the physical relationships among environmental changes, cloud changes and the TOA response.

Such a physically transparent approach has even broader implications. Communicating with the public about our confidence (or lack thereof) in clouds and climate change is hard. However, a physical theory of cloud feedbacks that can constrain, quantify and interpret models and observations, like the one proposed here, could help clear the cloud of uncertainty.

Online content

Any methods, additional references, Nature Portfolio reporting summaries, source data, extended data, supplementary information, acknowledgements, peer review information; details of author contributions and competing interests; and statements of data and code availability are available at <https://doi.org/10.1038/s41561-024-01414-4>.

References

- Ceppi, P. & Nowack, P. Observational evidence that cloud feedback amplifies global warming. *Proc. Natl Acad. Sci. USA* **118**, 2026290118 (2021).
- Myers, T. A. et al. Observational constraints on low cloud feedback reduce uncertainty of climate sensitivity. *Nat. Clim. Change* **11**, 501–507 (2021).
- Vogel, R. et al. Strong cloud–circulation coupling explains weak trade cumulus feedback. *Nature* **612**, 696–700 (2022).
- Sherwood, S. C. et al. An assessment of Earth's climate sensitivity using multiple lines of evidence. *Rev. Geophys.* **58**, 2019–000678 (2020).
- Forster, P. et al. The Earth's energy budget, climate feedbacks, and climate sensitivity. In *Climate Change 2021: The Physical Science Basis. Contribution of Working Group I to the Sixth Assessment Report of the Intergovernmental Panel on Climate Change* (eds Masson-Delmotte, V. et al.) 923–1054 (Cambridge Univ. Press, 2021).
- Ramanathan, V. & Collins, W. Thermodynamic regulation of ocean warming by cirrus clouds deduced from observations of the 1987 El Niño. *Nature* **351**, 27–32 (1991).
- Pierrehumbert, R. T. Thermostats, radiator fins, and the local runaway greenhouse. *J. Atmos. Sci.* **52**, 1784–1806 (1995).
- Lindzen, R. S., Chou, M.-D. & Hou, A. Y. Does the Earth have an adaptive infrared iris? *Bull. Am. Meteorol. Soc.* **82**, 417–432 (2001).
- Hartmann, D. L. & Michelsen, M. L. No evidence for iris. *Bull. Am. Meteorol. Soc.* **83**, 249–254 (2002).
- Mauritsen, T. & Stevens, B. Missing iris effect as a possible cause of muted hydrological change and high climate sensitivity in models. *Nat. Geosci.* **8**, 8–13 (2015).
- Hartmann, D. L. Tropical anvil clouds and climate sensitivity. *Proc. Natl Acad. Sci. USA* **113**, 8897–8899 (2016).
- Yoshimori, M., Lambert, F. H., Webb, M. J. & Andrews, T. Fixed anvil temperature feedback: positive, zero, or negative? *J. Clim.* **33**, 2719–2739 (2020).
- Fu, Q., Baker, M. & Hartmann, D. L. Tropical cirrus and water vapor: an effective Earth infrared iris feedback? *Atmos. Chem. Phys.* **2**, 31–37 (2002).

14. Lin, B., Wielicki, B. A., Chambers, L. H., Hu, Y. & Xu, K.-M. The iris hypothesis: a negative or positive cloud feedback? *J. Clim.* **15**, 3–7 (2002).
15. Zelinka, M. D., Klein, S. A., Qin, Y. & Myers, T. A. Evaluating climate models' cloud feedbacks against expert judgment. *J. Geophys. Res. Atmos.* **127**, e2021JDO35198 (2022).
16. Held, I. M. & Shell, K. M. Using relative humidity as a state variable in climate feedback analysis. *J. Clim.* **25**, 2578–2582 (2012).
17. Gasparini, B., Blossey, P. N., Hartmann, D. L., Lin, G. & Fan, J. What drives the life cycle of tropical anvil clouds? *J. Adv. Model. Earth Syst.* **11**, 2586–2605 (2019).
18. Beydoun, H., Caldwell, P. M., Hannah, W. M. & Donahue, A. S. Dissecting anvil cloud response to sea surface warming. *Geophys. Res. Lett.* **48**, e2021GL094049 (2021).
19. Jeevanjee, N. Three rules for the decrease of tropical convection with global warming. *J. Adv. Model. Earth Syst.* **14**, e2022MSO032852 (2022).
20. Zelinka, M. D. & Hartmann, D. L. Why is longwave cloud feedback positive? *J. Geophys. Res. Atmos.* **115**, D16117 (2010).
21. Bony, S. et al. Thermodynamic control of anvil cloud amount. *Proc. Natl Acad. Sci. USA* **113**, 8927–8932 (2016).
22. Saint-Lu, M., Bony, S. & Dufresne, J.-L. Observational evidence for a stability iris effect in the tropics. *Geophys. Res. Lett.* **47**, e2020GL089059 (2020).
23. Saint-Lu, M., Bony, S. & Dufresne, J.-L. Clear-sky control of anvils in response to increased CO₂ or surface warming or volcanic eruptions. *NPJ Clim. Atmos. Sci.* **5**, 78 (2022).
24. Ito, M. & Masunaga, H. Process-level assessment of the iris effect over tropical oceans. *Geophys. Res. Lett.* **49**, 2022–097997 (2022).
25. Stauffer, C. L. & Wing, A. A. Properties, changes, and controls of deep-convecting clouds in radiative–convective equilibrium. *J. Adv. Model. Earth Syst.* **14**, e2021MSO02917 (2022).
26. Ceppi, P., Brient, F., Zelinka, M. D. & Hartmann, D. L. Cloud feedback mechanisms and their representation in global climate models. *Wiley Interdiscip. Rev. Clim. Change* **8**, 465 (2017).
27. Lutsko, N. J., Sherwood, S. C. & Zhao, M. in *Clouds and Their Climatic Impacts: Radiation, Circulation, and Precipitation* (eds Sullivan, S. C. & Hoese, C.) 271–285 (AGU, 2023); <https://doi.org/10.1002/9781119700357.ch13>
28. Zelinka, M. D., Klein, S. A. & Hartmann, D. L. Computing and partitioning cloud feedbacks using cloud property histograms. part ii: attribution to changes in cloud amount, altitude, and optical depth. *J. Clim.* **25**, 3736–3754 (2012).
29. Li, R. L., Storelvmo, T., Fedorov, A. V. & Choi, Y.-S. A positive iris feedback: insights from climate simulations with temperature-sensitive cloud–rain conversion. *J. Clim.* **32**, 5305–5324 (2019).
30. Klein, S. A., Hall, A., Norris, J. R. & Pincus, R. Low-cloud feedbacks from cloud-controlling factors: a review. *Surv. Geophys.* **38**, 1307–1329 (2017).
31. Stevens, B., Sherwood, S. C., Bony, S. & Webb, M. J. Prospects for narrowing bounds on Earth's equilibrium climate sensitivity. *Earths Future* **4**, 512–522 (2016).
32. Fu, Q. & Liou, K. N. Parameterization of the radiative properties of cirrus clouds. *J. Atmos. Sci.* **50**, 2008–2025 (1993).
33. Siebesma, A. P., Bony, S., Jakob, C. & Stevens, B. *Clouds and Climate: Climate Science's Greatest Challenge* (Cambridge Univ. Press, 2020); <https://doi.org/10.1017/9781107447738>
34. McKim, B. A., Jeevanjee, N. & Vallis, G. K. Joint dependence of longwave feedback on surface temperature and relative humidity. *Geophys. Res. Lett.* **48**, 2021–094074 (2021).
35. Winker, D. M. et al. The calipso mission: a global 3D view of aerosols and clouds. *Bull. Am. Meteorol. Soc.* **91**, 1211–1230 (2010).
36. Loeb, N. G. et al. Clouds and the Earth's Radiant Energy System (CERES) Energy Balanced and Filled (EBAF) Top-of-Atmosphere (TOA) edition-4.0 data product. *J. Clim.* **31**, 895–918 (2018).
37. Morice, C. P. et al. An updated assessment of near-surface temperature change from 1850: the HadCRUT5 data set. *J. Geophys. Res. Atmos.* **126**, e2019JDO32361 (2021).
38. Hersbach, H. et al. The ERA5 global reanalysis. *Q. J. R. Meteorol. Soc.* **146**, 1999–2049 (2020).
39. Kiehl, J. T. On the observed near cancellation between longwave and shortwave cloud forcing in tropical regions. *J. Clim.* **7**, 559–565 (1994).
40. Hartmann, D. L. & Berry, S. E. The balanced radiative effect of tropical anvil clouds. *J. Geophys. Res. Atmos.* **122**, 5003–5020 (2017).
41. Jeevanjee, N. & Romps, D. M. Mean precipitation change from a deepening troposphere. *Proc. Natl Acad. Sci. USA* **115**, 11465–11470 (2018).
42. Wing, A. A. et al. Clouds and convective self-aggregation in a multimodel ensemble of radiative–convective equilibrium simulations. *J. Adv. Model. Earth Syst.* **12**, e2020MSO02138 (2020).
43. Fueglistaler, S. Observational evidence for two modes of coupling between sea surface temperatures, tropospheric temperature profile, and shortwave cloud radiative effect in the tropics. *Geophys. Res. Lett.* **46**, 9890–9898 (2019).
44. Deser, C. & Wallace, J. M. Large-scale atmospheric circulation features of warm and cold episodes in the tropical pacific. *J. Clim.* **3**, 1254–1281 (1990).
45. L'Ecuyer, T. S., Hang, Y., Matus, A. V. & Wang, Z. Reassessing the effect of cloud type on Earth's energy balance in the age of active spaceborne observations. part i: top of atmosphere and surface. *J. Clim.* **32**, 6197–6217 (2019).
46. Kubar, T. L. & Jiang, J. H. Net cloud thinning, low-level cloud diminishment, and Hadley circulation weakening of precipitating clouds with Tropical West Pacific SST using MISR and other satellite and reanalysis data. *Remote Sens.* **11**, 1250 (2019).
47. Igel, M. R., Drager, A. J. & Heever, S. C. A CloudSat cloud object partitioning technique and assessment and integration of deep convective anvil sensitivities to sea surface temperature. *J. Geophys. Res. Atmos.* **119**, 10515–10535 (2014).
48. Williams, I. N. & Pierrehumbert, R. T. Observational evidence against strongly stabilizing tropical cloud feedbacks. *Geophys. Res. Lett.* **44**, 1503–1510 (2017).
49. Bony, S. et al. Observed modulation of the tropical radiation budget by deep convective organization and lower-tropospheric stability. *AGU Adv.* **1**, e2019AV000155 (2020).
50. Kotarba, A. Z. & Solecki, M. Uncertainty assessment of the vertically-resolved cloud amount for joint CloudSat–CALIPSO radar–lidar observations. *Remote Sens.* **13**, 807 (2021).

Publisher's note Springer Nature remains neutral with regard to jurisdictional claims in published maps and institutional affiliations.

Open Access This article is licensed under a Creative Commons Attribution 4.0 International License, which permits use, sharing, adaptation, distribution and reproduction in any medium or format, as long as you give appropriate credit to the original author(s) and the source, provide a link to the Creative Commons licence, and indicate if changes were made. The images or other third party material in this article are included in the article's Creative Commons licence, unless indicated otherwise in a credit line to the material. If material is not included in the article's Creative Commons licence and your intended use is not permitted by statutory regulation or exceeds the permitted use, you will need to obtain permission directly from the copyright holder. To view a copy of this licence, visit <http://creativecommons.org/licenses/by/4.0/>.

© The Author(s) 2024

Methods

Conceptualizing cloud radiative effects

We start with an idealized model of cloud radiative effects at the TOA. Although tropical cloudiness is expected to be trimodal⁵¹, for simplicity we will consider a domain containing two cloud types: high clouds (h) and low clouds (l). (Many assessments of cloud feedbacks also use this bi-modal decomposition⁴.) Each type has an emission temperature (T_h, T_l), an optically thick cloud fraction (f_h, f_l) and an albedo (α_h, α_l) (Fig. 1). Mid-level clouds will be considered in our error analysis.

The TOA energy balance is $N = S - R$, where S is the absorbed short-wave radiation and R is the outgoing long-wave radiation. The cloud radiative effect C is the difference in N between all-sky and clear-sky (cs) conditions, $C = N - N_{cs}$ (ref. 52); C can be decomposed into long-wave and short-wave components: $C = C^{sw} + C^{lw}$.

In the long-wave component, clear-sky regions with a surface temperature T_s will emit to space with an outgoing long-wave radiation of $R_{cs}^{T_s}$, but a portion will be blocked by clouds. Long-wave emissivity will not be considered because most clouds have an emissivity close to one³². Assuming random overlap between high clouds and low clouds⁵³, the domain-averaged clear-sky contribution is $R_{cs}^{T_s}(1 - f_h)(1 - f_l)$. Low clouds are so close to the surface that we treat their emission to space like clear-sky surface emission but at T_l . Their domain-averaged contribution is $R_{cs}^{T_l}f_l(1 - f_h)$. Since $R_{cs}^{T_s}$ is an approximately linear function of temperature⁵⁴, $R_{cs}^{T_l} \approx R_{cs}^{T_s} + \lambda_{cs}(T_s - T_l)$, where $\lambda_{cs} \equiv -dR_{cs}/dT_s \approx -2 \text{ W m}^{-2} \text{ K}^{-1}$ is a representative value for the long-wave clear-sky feedback³⁴. We assume that high clouds are so high that they emit directly to space³³ with a value $\sigma T_h^4 f_h$. Summing these contributions, the domain-averaged outgoing long-wave radiation is

$$R = R_{cs}^{T_s}(1 - f_h) + \sigma T_h^4 f_h + \lambda_{cs}(T_s - T_l)(1 - f_h)f_l, \quad (14)$$

and the long-wave cloud radiative effect $-(R - R_{cs})$ is

$$C^{lw} = R_{cs}^{T_s}f_h - \sigma T_h^4 f_h - \lambda_{cs}(T_s - T_l)(1 - f_h)f_l. \quad (15)$$

In the short-wave component, there is an incoming solar radiation S^\downarrow , and we assume that there is no absorption except at the surface. High clouds reflect a portion $\alpha_h f_h$ back to space. The transmitted radiation then hits low clouds, which reflect a portion $\alpha_l f_l$ back to space (ignoring secondary reflections with the anvils above). The transmitted radiation then hits the surface, which reflects a portion α_s back out to space and absorbs the rest. Summing these contributions, the domain-averaged absorbed short-wave radiation at TOA is

$$S = S^\downarrow(1 - \alpha_h f_h)(1 - \alpha_l f_l)(1 - \alpha_s). \quad (16)$$

The TOA-absorbed short-wave in clear skies is $S_{cs} = S^\downarrow(1 - \alpha_s)$, so the short-wave cloud radiative effect $(S - S_{cs})$ is:

$$C^{sw} = S_{cs}(-\alpha_h f_h - \alpha_l f_l + \alpha_h \alpha_l f_h f_l). \quad (17)$$

It will prove helpful to separate the contribution of isolated high clouds and isolated low clouds to the net cloud radiative C . Setting $f_l = 0$ yields the isolated high-cloud radiative effect:

$$C_h = (-S_{cs}\alpha_h + R_{cs}^{T_s} - \sigma T_h^4)f_h. \quad (18)$$

Setting $f_h = 0$ yields the isolated low-cloud radiative effect:

$$C_l = (-S_{cs}\alpha_l - \lambda_{cs}(T_s - T_l))f_l. \quad (19)$$

The total cloud radiative effect C in terms of each cloud is:

$$C = C_h + C_l + m_{eh}, \quad (20)$$

where

$$m_{eh} = (S_{cs}\alpha_l\alpha_h + \lambda_{cs}(T_s - T_l))f_l f_h, \quad (21)$$

represents the cloud-overlap masking effect. Note that $C_h \propto f_h$, $C_l \propto f_l$ and $m_{eh} \propto f_l f_h$.

Feedback decomposition

We will now derive various cloud feedbacks from these equations and assume a fixed relative humidity. The lapse-rate feedback has been shown to be small when using this reference response^{16,55}, so it will be ignored here.

$$\begin{aligned} \lambda &\equiv \frac{dN}{dT_s} \\ &= \frac{S_{cs}}{dT_s} - \frac{dR_{cs}^{T_s}}{dT_s} + \frac{dC}{dT_s} \\ &= \lambda_{cs}(1 - f_h) \\ &\quad + (R_{cs}^{T_s} - \sigma T_h^4 + \lambda_{cs}(T_s - T_l)f_l - S_{cs}\alpha_h + S_{cs}\alpha_h\alpha_l f_l) \frac{df_h}{dT_s} \\ &\quad + (-\lambda_{cs}(T_s - T_l)(1 - f_h) - S_{cs}\alpha_l + S_{cs}\alpha_h f_h \alpha_l) \frac{df_l}{dT_s} \\ &\quad + -4\sigma T_h^3 f_h \frac{dT_h}{dT_s} \\ &\quad + -\lambda_{cs}(1 - f_h)f_l \frac{d(T_s - T_l)}{dT_s} \\ &\quad + (-S_{cs}f_h + S_{cs}f_h\alpha_l f_l) \frac{d\alpha_h}{dT_s} \\ &\quad + (-S_{cs}f_l + S_{cs}\alpha_h f_h f_l) \frac{d\alpha_l}{dT_s} \\ &\quad - S^\downarrow(1 - \alpha_h f_h)(1 - \alpha_l f_l) \frac{d\alpha_s}{dT_s} \\ &\quad - (T_s - T_l)(1 - f_h)f_l \frac{d\lambda_{cs}}{dT_s}. \end{aligned} \quad (22)$$

Recognizing that many of these terms can be rewritten as cloud radiative effects, we get:

$$\begin{aligned} \lambda &= \lambda_{cs}(1 - f_h) \\ &\quad + (C_h + m_{eh}) \frac{d \ln f_h}{dT_s} \\ &\quad + (C_l + m_{eh}) \frac{d \ln f_l}{dT_s} \\ &\quad - 4\sigma T_h^3 f_h \frac{dT_h}{dT_s} \\ &\quad - \lambda_{cs}(1 - f_h)f_l \frac{d(T_s - T_l)}{dT_s} \\ &\quad + (C_h^{sw} + m_{eh}^{sw}) \frac{d \ln \alpha_h}{dT_s} \\ &\quad + (C_l^{sw} + m_{eh}^{sw}) \frac{d \ln \alpha_l}{dT_s} \\ &\quad + C_s \frac{d \ln \alpha_s}{dT_s}, \end{aligned} \quad (23)$$

where we have assumed that $d\lambda_{cs}/dT_s$ is negligible, and $C_s = -S^\downarrow(1 - \alpha_h f_h)(1 - \alpha_l f_l)\alpha_s$ is the surface albedo radiative effect, which is equivalent to the 'cryosphere radiative forcing'⁵⁶.

Now we name and then describe each term:

$$\lambda = \lambda_0 + \lambda_h^{\text{area}} + \lambda_l^{\text{area}} + \lambda_h^{\text{temp}} + \lambda_l^{\text{temp}} + \lambda_h^{\text{albedo}} + \lambda_l^{\text{albedo}} + \lambda_s^{\text{albedo}} \quad (24)$$

where λ_0 is the anvil cloud-masked long-wave clear-sky feedback. It is our null hypothesis for the climate response to warming because it assumes fixed relative humidity; fixed anvil temperature, area and albedo; fixed low-cloud temperature difference, area and albedo; and fixed surface albedo; λ_h^{area} and λ_l^{area} are the feedbacks from a changing anvil cloud and low-cloud area, respectively; λ_h^{temp} is the feedback from a changing anvil cloud temperature; λ_l^{temp} is the feedback from a changing temperature difference between low clouds and the surface; $\lambda_h^{\text{albedo}}$,

$\lambda_e^{\text{albedo}}$ and $\lambda_s^{\text{albedo}}$ are the feedbacks from a changing albedo of anvil clouds, low clouds and surface, respectively. We omit the surface albedo feedback from equation (2) because we are interested in tropical climate.

For simplicity, we have assumed that cloud emissivities of high clouds and low clouds (ϵ_h, ϵ_l) are equal to one³². However, if we relax this assumption for completeness, one can show this leads to a high-cloud and low-cloud emissivity feedback with the following forms:

$$\begin{aligned} \lambda_h^{\text{emissivity}} &= (C_h^{\text{lw}} + m_{\text{th}}^{\text{lw}}) \frac{d \ln \epsilon_h}{dT_s}, \\ \lambda_e^{\text{emissivity}} &= (C_e^{\text{lw}} + m_{\text{th}}^{\text{lw}}) \frac{d \ln \epsilon_e}{dT_s}, \end{aligned} \quad (25)$$

which closely resemble the form of the cloud albedo feedback. Some of the other feedbacks will have small modifications, but they are unimportant here.

Climatology

We combine monthly mean satellite observations, surface temperature measurements and reanalysis and re-grid all datasets onto a common 2° latitude × 2.5° longitude grid over the tropical belt (30° N–30° S) from June 2006 to December 2016. Although anvil clouds populate the globe⁵⁷, it is less clear how extratropical anvils change with warming. Most cloud feedback assessments consider only tropical anvil clouds, so we will follow this convention.

From the CALIPSO lidar satellite dataset³⁵, we obtain vertical profiles of cloud fraction for optical depths of $0.3 \leq \tau \leq 5.0$. This range excludes both deep convective cores and optically thin cirrus unconnected to deep convection²². We then vertically smooth the native vertical 60 m resolution profiles with a 480 m running mean. For anvil detection, we consider ice-cloud data above 8 km. For shallower clouds, we consider the sum of ice and liquid cloud fraction data below 8 km. The diagnosed cloud fractions are the absolute maximum of the profile in their respective domains, but if the identified maximum does not exceed a cut-off ($f_{\text{cut}} = 0.03$), then that region is considered to be clear sky ($f = 0$). This algorithm is applied to every grid point and then tropically averaged. Our approach thus far resembles that of ref. 22, just extended to include low clouds.

To match the inferred cloud radiative effects with the observed, we consider an effective cloud fraction $f_h = n \times \text{Max}(f(z))$ for high clouds, where n is a single tuned parameter to account for collapsing the high-cloud profile into one level. This accounting is more important for high clouds, as their profile's full width–half maximum is ~5 km (Extended Data Fig. 1), whereas low clouds are already localized with a full width–half maximum of ~1 km (Extended Data Fig. 1). While n could be more rigorously derived from detailed considerations of cloud overlap⁵³, we opt to determine n by fitting the predicted tropical- and time-averaged long-wave cloud radiative effect C^{lw} to its observed counterpart $C_{\text{obs}}^{\text{lw}}$ from CERES (see Cloud fraction section). Doing so yields a spatially and temporally constant value of $n = 1.7$. This value lies between that from assuming maximum overlap between each layer of the anvil cloud, which yields $n = 1$, and random overlap, which yields $n \approx 5$.

The height of the diagnosed maximum cloud fraction is then used to diagnose the cloud temperatures T_h, T_l at each space and time by selecting the corresponding atmospheric temperature in ERA5 reanalysis³⁸. We use the HadCRUT5 dataset³⁷ to diagnose the surface temperature T_s .

We use monthly mean TOA radiative fluxes, both clear sky and all sky, from the CERES satellite EBAF Ed4.1 product^{36,58}. We diagnose the surface albedo α_s as the ratio of upwelling clear-sky short-wave radiation S_{cs}^{\uparrow} to incoming short-wave radiation S^{\downarrow} . However, because short-wave absorption and scattering occurs in the real atmosphere, our surface albedo is more accurately characterized as the planetary clear-sky albedo⁵⁹. We diagnose the cloud albedos by assuming that

they are constant in space and by fitting the predicted tropical- and time-averaged short-wave cloud radiative effect C^{sw} to its observed counterpart $C_{\text{obs}}^{\text{sw}}$ from CERES. With two unknowns, we must provide two constraints. We do this by splitting the tropics into two distinct dynamical regimes on the basis of a threshold of 500 hPa midtropospheric velocity $\omega_{500} = 25 \text{ hPa day}^{-1}$ obtained from monthly ERA5 reanalysis data. These regions are treated as independent so that they provide two constraints. The regime-averaged short-wave radiative effect is then fitted to its observed counterpart by using the fsolve function from the scipy.optimize python module. (The precise threshold of 25 hPa day⁻¹ was chosen because it resulted in the smallest root mean square error between C^{sw} and $C_{\text{obs}}^{\text{sw}}$).

Cloud fraction

We use the CALIPSO Lidar Satellite CAL_LID_L3_Cloud_Occurrence-Standard-V1-00 data product⁶⁰, the same dataset used in ref. 22. While the high-cloud fraction could simply be diagnosed as the maximum cloud fraction of the profile ($f_h = \text{Max}(f(z))$), the calculated long-wave cloud radiative effect C^{lw} will not match with observations. To rectify this, we consider using a single tuning parameter, n . That is, we have an effective cloud fraction $f_h = n \times \text{Max}(f(z))$ that accounts for representing a cloud profile with a single level.

We first demand that n be constant with space and time to ensure that areal changes (changes in f_h) are not artificially convolved with vertical changes that relate to optical depth and albedo (α). This decision projects the spatio-temporal variability in the vertical extent of anvils more onto α than onto f_h .

We then fit the predicted tropically and temporally averaged long-wave radiative effect C^{lw} to its observed counterpart $C_{\text{obs}}^{\text{lw}}$ from CERES. Given these constraints, and the inputs to equation (15), n can be solved for as

$$n = \frac{\langle C_{\text{obs}}^{\text{lw}} + \lambda_{\text{cs}}(T_s - T_e)f_e \rangle}{\langle R_{\text{cs}} \text{max}(f(z)) - \sigma T_h^4 \text{max}(f(z)) + \lambda_{\text{cs}}(T_s - T_e)f_e \text{max}(f(z)) \rangle}, \quad (26)$$

where $\langle \cdot \rangle$ denotes a tropical and temporal average.

When plotting the scatter of $\ln f_h$ against T_s in Fig. 4, grid cells with $f_h = 0$ are excluded to avoid logarithmic divergences.

Uncertainty analysis for area feedback

Uncertainty in our estimates of $d \ln f_h / dT_s$ and $C_h + m_{\text{th}}$ translate to uncertainty in λ_h^{area} . As stated in the main text, we estimate $d \ln f_h / dT_s = -4 \pm 2\% \text{ K}^{-1}$. For the anvil cloud radiative effect, we found $C_h + m_{\text{th}} = -1.5 \text{ W m}^{-2}$. However, other observational studies have found it to be -4 W m^{-2} (ref. 40), 0.6 W m^{-2} (ref. 17) and 2 W m^{-2} (ref. 45). This is probably due to methodological differences and the fact that anvil clouds have no precise definition. Furthermore, CERES TOA monthly fluxes have a stated uncertainty of 2.5 W m^{-2} (ref. 36).

Another source of error comes from neglecting mid-level clouds, a fairly common cloud type⁵¹, as their own identities. Let us assume that emissions from mid-level congestus clouds (c) experience a clear-sky greenhouse effect. By symmetry with low clouds, they should contribute an additional cloud-overlap masking term that appears in our expression for $\lambda_{\text{area}}^{\text{area}}$: $m_{\text{ch}} = (S_{\text{cs}} \alpha_c \alpha_h + \lambda_{\text{cs}}(T_s - T_c))f_c f_h$. Assuming that $f_c = 0.1, f_h = 0.17, \alpha_c = \alpha_h = 0.45, T_c = 250 \text{ K}, T_s = 298 \text{ K}, S_{\text{cs}} = 347 \text{ W m}^{-2}, \lambda_{\text{cs}} = -2 \text{ W m}^{-1} \text{ K}^{-1}$ yields $m_{\text{ch}} \approx -0.5 \text{ W m}^{-2}$.

We therefore estimate $C_h + m_{\text{th}} = -1 \pm 3 \text{ W m}^{-2}$. This results in our best estimate of the anvil cloud area feedback:

$$\begin{aligned} \langle \lambda_h^{\text{area}} \rangle &= 1/2 \times (-4 \pm 2\% \text{ K}^{-1}) \times (-1 \pm 3 \text{ W m}^{-2}) \\ &= 0.02 \pm 0.07 \text{ W m}^{-2} \text{ K}^{-1}. \end{aligned} \quad (27)$$

Further uses of our framework

Our feedback expressions might also provide a quick, quantitative and physically transparent way to interpret how model biases influence

feedbacks. For example, if members of a General Circulation Model ensemble simulate C_h between $\pm 10 \text{ W m}^{-2}$ but they all simulate the same $d \ln f_h / dT_s = -4\% \text{ K}^{-1}$, then their area feedbacks will range between $\mp 0.2 \text{ W m}^{-2} \text{ K}^{-1}$. If all ensemble members simulate $C_h = 1 \text{ W m}^{-2}$, but simulate $d \ln f_h / dT_s = \pm 5\% \text{ K}^{-1}$, then their area feedbacks will range between $\pm 0.03 \text{ W m}^{-2} \text{ K}^{-1}$. This quantitative yet clear diagnostic could provide testable hypotheses that advance our understanding and development of models.

Data availability

CERES data were obtained from the NASA Langley Research Center (<https://ceres.larc.nasa.gov/data/>). CALIPSO/CLOUDSAT data were obtained from NASA Atmospheric Science Data Center (https://asdc.larc.nasa.gov/project/CALIPSO/CAL_LID_L3_Cloud_Occurrence-Standard-V1-00_V1-00). ERA5 reanalysis data were obtained from the Copernicus Climate Change Service (<https://cds.climate.copernicus.eu/>). HadCRUT5 data were obtained from the Met Office Hadley Centre (<https://www.metoffice.gov.uk/hadobs/hadcrut5/data/HadCRUT.5.0.2.0/download.html>).

Code availability

Scripts used to support the analysis of satellite and reanalysis data are available at <https://github.com/mckimb/anvil-area-feedback> and https://nbviewer.org/github/mckimb/anvil-area-feedback/blob/main/github_plotting.ipynb.

References

51. Johnson, R. H., Rickenbach, T. M., Rutledge, S. A., Ciesielski, P. E. & Schubert, W. H. Trimodal characteristics of tropical convection. *J. Clim.* **12**, 2397–2418 (1999).
52. Coakley, J. A. & Baldwin, D. G. Towards the objective analysis of clouds from satellite imagery data. *J. Appl. Meteorol. Climatol.* **23**, 1065–1099 (1984).
53. Oreopoulos, L., Cho, N. & Lee, D. Revisiting cloud overlap with a merged dataset of liquid and ice cloud extinction from CloudSat and CALIPSO. *Front. Remote Sens.* **3**, 1076471 (2022).
54. Koll, D. D. B. & Cronin, T. W. Earth's outgoing longwave radiation linear due to H_2O greenhouse effect. *Proc. Natl Acad. Sci. USA* **115**, 10293–10298 (2018).
55. Zelinka, M. D. et al. Causes of higher climate sensitivity in CMIP6 models. *Geophys. Res. Lett.* **47**, 2019–085782 (2020).
56. Flanner, M. G., Shell, K. M., Barlage, M., Perovich, D. K. & Tschudi, M. A. Radiative forcing and albedo feedback from the Northern Hemisphere cryosphere between 1979 and 2008. *Nat. Geosci.* **4**, 151–155 (2011).
57. Thompson, D. W. J., Bony, S. & Li, Y. Thermodynamic constraint on the depth of the global tropospheric circulation. *Proc. Natl Acad. Sci. USA* **114**, 8181–8186 (2017).
58. Loeb, N. G. et al. Toward a consistent definition between satellite and model clear-sky radiative fluxes. *J. Clim.* **33**, 61–75 (2020).
59. Chen, T. S. & Ohring, G. On the relationship between clear-sky planetary and surface albedos. *J. Atmos. Sci.* **41**, 156–158 (1984).
60. CALIPSO Lidar Level 3 Cloud Occurrence Data, Standard V1-00 (NASA, 2018); https://doi.org/10.5067/CALIP/CALIPSO/L3_CLOUD_OCCURRENCE-STANDARD-V1-00

Acknowledgements

We thank G. George for illustrating the clouds in Fig. 1 and A. Sokol, D. Hartmann, M. Saint-Lu, B. Gasparini, I. Simpson, D. Randall and B. Stevens for helpful conversations. The Franco-American Fulbright Commission (B.A.M.) and EU Horizon 2020 grant agreement 820829 "CONSTRAIN" (S.B. and J.-L.D.) supported this work.

Author contributions

B.M. and S.B. designed research; B.M. performed research. B.M., S.B. and J.-L.D. analysed data; and B.M. wrote the paper.

Competing interests

The authors declare no competing interests.

Additional information

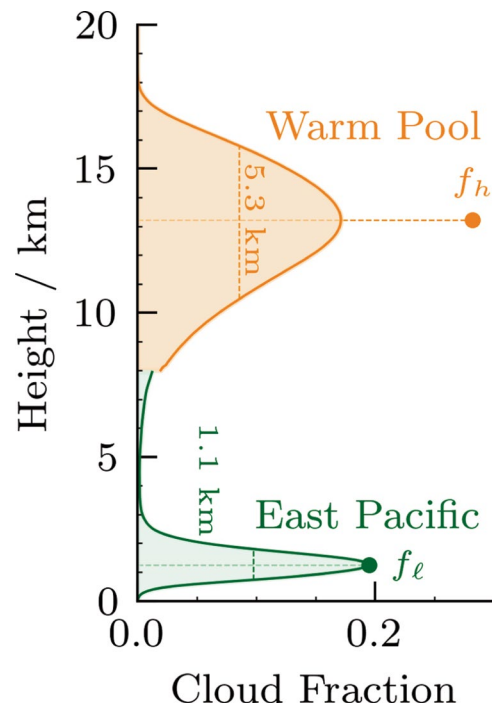
Extended data is available for this paper at <https://doi.org/10.1038/s41561-024-01414-4>.

Supplementary information The online version contains supplementary material available at <https://doi.org/10.1038/s41561-024-01414-4>.

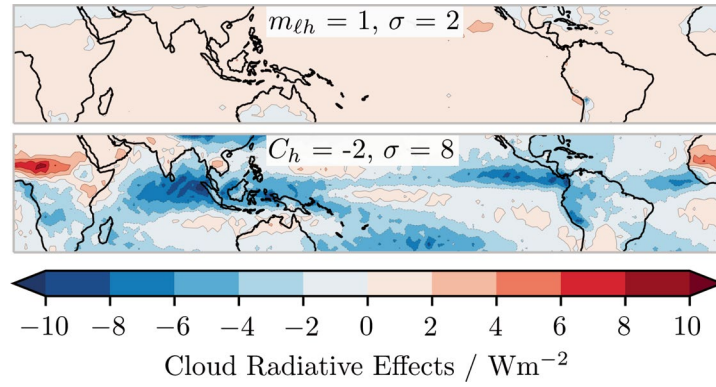
Correspondence and requests for materials should be addressed to Brett McKim.

Peer review information *Nature Geoscience* thanks Stephen Klein, Trude Storelvmo and Sylvia Sullivan for their contribution to the peer review of this work. Primary Handling Editor: Tom Richardson, in collaboration with the *Nature Geoscience* team.

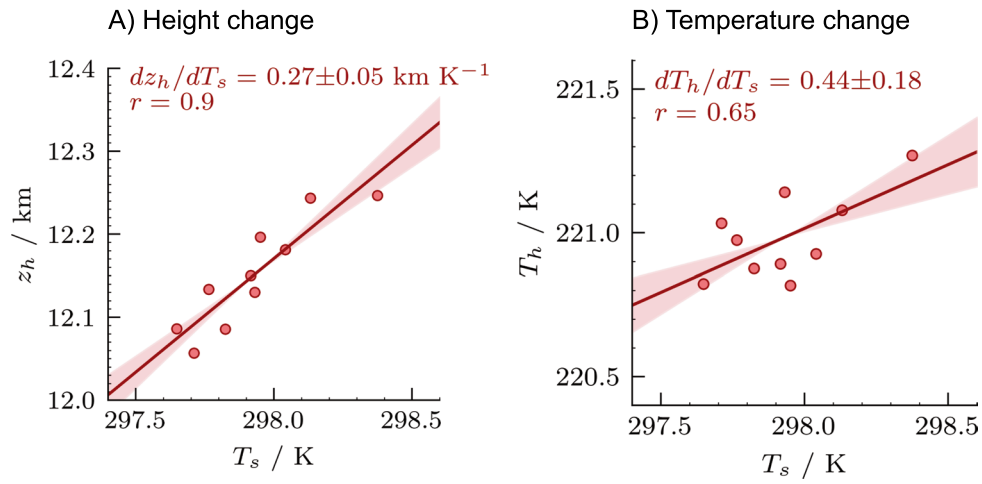
Reprints and permissions information is available at www.nature.com/reprints.



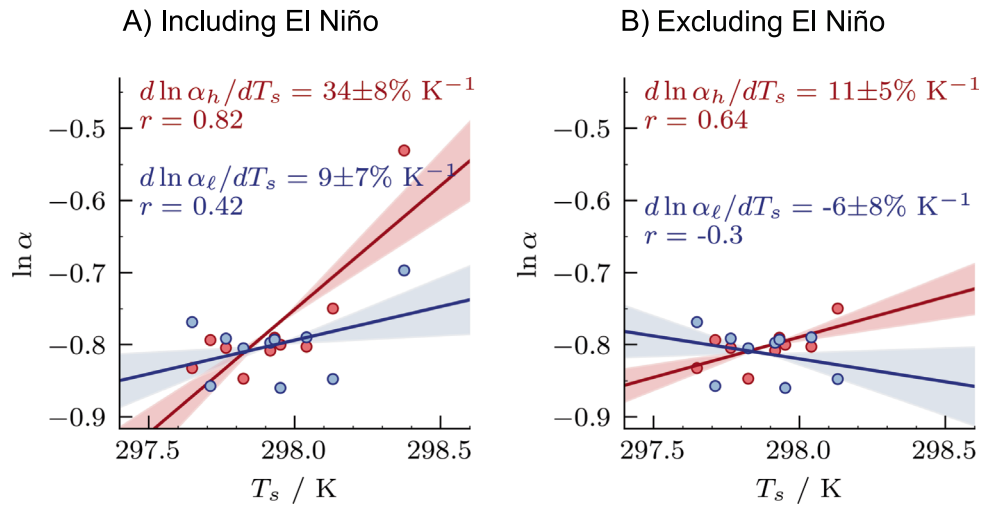
Extended Data Fig. 1 | Illustration of effective cloud fraction. The high cloud fraction profile in the Warm Pool and low cloud fraction profile in the East Pacific are from CALIPSO. The full width-half maximum and effective cloud fraction of each profile are shown. The high cloud and low cloud profiles are clipped below 8 km and above 4 km, respectively, in accordance with our detection method.



Extended Data Fig. 2 | Climatological value of tropical quantities. Top) Inferred cloud-overlap effect from Equation (21). Bottom) Inferred anvil cloud radiative effect from Equation (18). Tropical mean values and standard deviations are shown in the upper middle of each panel. Refer to Fig. 2 to see m_{lh} and C_h and other quantities plotted with a broader color scale.



Extended Data Fig. 3 | Interannual changes in tropical mean anvil cloud height (a) and temperature (b). In each subplot, the slope, correlation for the best fit line and its standard error are shown. Standard error in the slope due to limited sampling is indicated by shading.



Extended Data Fig. 4 | Interannual changes in tropical mean anvil cloud albedo (red) and low cloud albedo (blue). (a) The line of best fit is calculated with the 2015–2016 El Niño included. (b) The line of best fit is calculated without the El Niño.

Extended Data Table 1 | Climatological value of tropical quantities used in this study

Quantity	Description	Tropical mean value	Derivation
f_h	Anvil cloud area fraction	0.16	CALIPSO
f_ℓ	Low cloud area fraction	0.11	CALIPSO
T_h	Anvil temperature	221 K	ERA5
T_ℓ	Low cloud temperature	287 K	ERA5
T_s	Surface temperature	298 K	HadCRUT5
α_s	Planetary surface albedo	0.13	CERES
S^\downarrow	Incoming shortwave radiation	398 Wm^{-2}	CERES
S_{cs}	Clear-sky absorbed shortwave	347 Wm^{-2}	CERES
R_{cs}	Clear-sky outgoing longwave	287 Wm^{-2}	CERES
n	Effective cloud fraction scaling	1.7	Fitted from C_{obs}^{lw}
α_h	Anvil albedo	0.45	Fitted from C_{obs}^{sw}
α_ℓ	Low cloud albedo	0.45	Fitted from C_{obs}^{sw}
C	Net cloud radiative effect	-15.6 Wm^{-2}	Inferred
C^{sw}	Shortwave cloud radiative effect	-42.6 Wm^{-2}	Inferred
C^{lw}	Longwave cloud radiative effect	27.0 Wm^{-2}	Inferred
C_h	Anvil cloud radiative effect	-2.0 Wm^{-2}	Inferred
C_h^{sw}	Shortwave anvil cloud radiative effect	-26.1 Wm^{-2}	Inferred
C_h^{lw}	Longwave anvil cloud radiative effect	24.1 Wm^{-2}	Inferred
C_ℓ	Low cloud radiative effect	-14.3 Wm^{-2}	Inferred
C_ℓ^{sw}	Shortwave low cloud radiative effect	-17.3 Wm^{-2}	Inferred
C_ℓ^{lw}	Longwave low cloud radiative effect	3.1 Wm^{-2}	Inferred
$m_{\ell h}$	Cloud overlap effect	0.6 Wm^{-2}	Inferred
$m_{\ell h}^{sw}$	Shortwave cloud overlap effect	1.1 Wm^{-2}	Inferred
$m_{\ell h}^{lw}$	Longwave cloud overlap effect	-0.5 Wm^{-2}	Inferred

All radiative quantities are evaluated at the top of atmosphere. C_{obs}^{lw} and C_{obs}^{sw} refer to the observed longwave and shortwave cloud radiative effects from CERES. See Climatology section for details.